1 # Strain-Engineered Manufacturing of Freeform Carbon Nanotube
2 # Microstructures

3 *M. De Volder[1,2,*,†], S. Park[3,4,*], S. Tawfick[3,4,5], A.J. Hart[3,4,†]*

4 [1] *Institute for Manufacturing, University of Cambridge, 17 Charles Babbage Rd, Cambridge, CB3*
5 *0FS, UK*

6 [2] *IMEC, Kapeldreef 75, 3001 Heverlee, Belgium, Department of Mechanical Engineering, Katholieke*
7 *Universiteit Leuven, 3001 Leuven, Belgium*

8 [3] *Mechanosynthesis Group, Department of Mechanical Engineering, University of Michigan, 2350*
9 *Hayward Street, Ann Arbor, Michigan 48109 USA*

10 [4] *Mechanosynthesis Group, Department of Mechanical Engineering, Massachusetts Institute of*
11 *Technology, 77 Massachusetts Ave, Cambridge, Massachusetts, 02139 USA*

12 [5] *Mechanical Science and Engineering, University of Illinois at Urbana Champaign, Urbana, Illinois,*
13 *61822 USA*

14 **These authors contributed equally.*

15 [†] *Corresponding authors: M. De Volder: mfld2@cam.ac.uk, A.J. Hart: ajhart@mit.edu*

16

17 ## Abstract

18 The skins of many plants and animals have intricate micro-scale surface features that give rise to
19 properties such as directed water repellency and adhesion, resistance to fouling, and camouflaging.
20 However, engineered mimicry of these designs has been limited by the capabilities of creating
21 complex forms by top-down fabrication processes. We demonstrate a new technique for scalable
22 manufacturing of freeform microstructures, via strain-engineered growth of aligned carbon nanotubes
23 (CNTs). Lithographic patterning of the CNT growth catalyst is used to locally modulate the CNT
24 growth rate, which causes collective bending during growth with exceptional uniformity. The final
25 shape of the curved CNT microstructures can be approximated via finite element modeling, and
26 compound catalyst shapes produce microstructures with multi-directional curvature and unusual self-
27 organized patterns. Conformal coating of the CNTs enables tuning of the mechanical properties
28 independently from the microstructure geometry, representing a versatile principle for design and
29 manufacturing of complex microstructured surfaces.

30

31

32

33

1

Introduction

Scalable fabrication of microstructures that mimic the hierarchical surface designs found in nature has been a long-standing aspiration of material scientists [1-5]. While symbiotic growth of the integrated circuit (IC) and micro electro mechanical systems (MEMS) industries has enabled innovations in 3D fabrication that leverage semiconductor processing tools, these methods, such as interference or inclined exposure lithography are typically limited to arrays of identical structures [6-8]. Rapid prototyping methods such as direct laser writing, multiphoton lithography, and focused ion beam milling can create arbitrary forms but are serial, and therefore have lower areal throughput [9, 10]. It is also especially difficult to fabricate surface structures having curved and/or re-entrant geometries.

On the other hand, use of locally directed actions, such as mechanical stresses, capillary forces, and electromagnetic fields, along with their interactions with templates, offers opportunity to create novel self-organized geometries and to design fabrication processes that achieve attractive combinations of dimensional control and throughput [2, 8, 11-15]. Examples abound in soft materials and chemical systems including micro-scale reaction-diffusion patterns [16, 17], self-assembly of block copolymers [18], and helical aggregation of polymer nanopillars [19, 20]. However, many of these processes need further development to achieve structural uniformity over large substrates.

We present a novel approach taking advantage of microscale top-down lithographic patterning in conjunction with nanoscale self-organization, which enables large-area fabrication of freeform microstructures made of aligned carbon nanotubes (CNTs). This process leverages the influence of the catalyst-substrate interactions on the growth rate of CNTs [21], creating stress gradients during synthesis that guide the CNTs into curved microscale geometries. Our method is analogous to the well-known use of thin film stress to create curved and folded MEMS structures [22]. However, because our process is based on an additive chemical synthesis process instead of a subtractive etching and release technique, it enables the direct synthesis of complex microstructures that are perpendicular rather than parallel to the substrate. This has two major implications: it enables fabrication of closely packed arrays of structures with heterogeneous shapes, and the porosity of the CNT forests enables conformal coating after growth to modify chemical and/or mechanical properties. We demonstrate this latter point by conformal coating of CNT "microtruss" arrays by atomic layer deposition (ALD) and polymer CVD, which increases their mechanical stiffness without changing the geometry.

Results

Fabrication. CNTs grown by chemical vapour deposition (CVD) from a high-density arrangement of catalyst nanoparticles on a substrate are known to self-organize into vertically aligned assemblies often called "CNT forests" [23, 24]. We first observed that the density and rate of CNT forest growth from a widely studied supported catalyst (Fe/Al_2O_3, 1/10 nm) can be influenced by the material immediately beneath the catalyst. This premise is shown in **Fig. 1a**; patterning of CNT growth catalyst (Fe/Al_2O_3) on a SiO_2/TiN "checkerboard" followed by exposure to standard CVD conditions (see Methods) results in a "bi-level" CNT micropillar array. The catalyst patterns directly on SiO_2 grow CNTs to ~100 μm (in < 2 minutes), whereas the patterns on TiN (upon SiO_2) grow CNTs to 50 μm in the same time span. In **Fig. 1b**, "tri-level" CNT forests are grown by arranging patches of catalyst on SiO_2, 70 nm TiN, and 140 nm TiN. This principle could be extended to an arbitrary number of levels or even continuous height gradients via additional lithography and underlayer deposition steps that modulate the growth rate via catalyst-substrate interactions.

Next, we used the above differential growth principle to design compound catalyst/underlayer patterns that directly form curved CNT forest geometries. If a continuous micro-scale catalyst pattern is placed partially on SiO_2 and partially on TiN, the differential growth rates induce stress within the CNT microstructure. For example, as shown in **Fig. 2a and 2b**, a square catalyst pattern with half of its area on the TiN layer bends toward the side which is upon TiN, due to the difference in growth rate on the coupled halves of the structure. The stress is transferred between contacting CNTs at the boundary region via mechanical entanglement and van der Waals interactions among the CNTs. Depending on the curvature and length of the structures, slanted micropillars (**Fig. 2a**), or arches (**Fig. 2b**) can be fabricated. Because the local interaction and differential growth rate determines the trajectory of each structure, large arrays with nearly identical anisotropic shapes can be produced as shown in the SEM images. Importantly, these 3D structures are fabricated using only two standard photolithography steps, one for patterning the TiN layer, and one for patterning the catalyst layer.

The curvature can be controlled by designing the amount of overlap between the catalyst and the TiN underlayer. This is illustrated in **Fig. 3a and b,** which respectively show arrays of round and square cross-section micropillars where the overlap distance is varied from left to right (increments of 5 μm). As expected, the portion of the pillars growing on TiN is always shorter, and as a result, all pillars bend towards the TiN side. As the portion of overlap decreases, the stress induced by the differential growth rate causes increased bending (smaller radius of curvature), reaching a maximum when the catalyst shape is split symmetrically by the TiN layer. With <50% overlap on TiN, the curvature increases gradually until the structure is only slightly curved at the rightmost extent of the array. The CNTs are generally tangential to the curvature of the microstructures, similar to the CNT alignment observed in CNT forests.

100 **Static model of stress-driven CNT curvature.** The coupling of stress and CNT growth rate, via

101 the anisotropic mechanics of the CNT forest [25], is a complex problem. However, we find that a

102 static mechanical model analogous to that used for differential expansion of a bi-material cantilever

103 beam can reasonably predict the curvature of CNT structures grown from an overlapped catalyst/TiN

104 rectangle. Starting from the classical formulation of the bimetallic strip model [26], we replace the

105 temperature-dependent expansion term by a differential lengthening term representing the CNT

106 growth rate. Accordingly, the curvature of the compound CNT microstructure is described as:

107
$$\frac{1}{\rho} = \frac{6\left(\frac{R_1 - R_2}{R_1}\right)(1+m)^2}{w\left(3(1+m)^2 + (1+mn)\left(m^2 + \frac{1}{mn}\right)\right)} \qquad (1)$$

108 Here ρ is the radius of curvature, R_1 and R_2 are the growth rates (1 denotes CNTs on Fe/Al$_2$O$_3$/SiO$_2$

109 and 2 denotes CNTs on Fe//Al$_2$O$_3$/TiN), and w is the CNT micropillar width. In addition, m and n are

110 defined as

111 $m = \frac{w_2}{w_1}, n = \frac{E_2}{E_1} \qquad (2)$

112 where w denotes the width and E denotes the respective Young's Moduli of the segments . The value

113 of n is specified as 0.6 which is the ratio of the measured areal mass density of CNTs on the respective

114 underlayers; however, because the elongation of each layer is specified in the model, the output is

115 insensitive to this value. The geometric parameters are defined in **Fig. 3c**.

116 Using the calculated curvatures, and the weighted average growth rate, the shapes of the resultant

117 CNT microstructures were visualized using Matlab. The simulation results correspond to the rows of

118 structures in the SEM image **Fig. 3b**. To compare the experiments to the simulation, the tip position

119 was characterized in horizontal and vertical axes, normalized to the base dimension (w) , as shown in

120 **Fig. 3c**. For both the experiment and simulation, the x position of the tip reaches its maximum at 0.4

121 overlap, and the y position reaches its minimum at approximately 0.6-0.7 overlap.

122 The differences between the predicted and calculated displacements arise because the model does

123 not capture the exact kinetics of CNT growth, which varies with time. Moreover, it cannot consider

124 how the stress between the two portions of the structure, which are idealized as perfectly coupled

125 without slip, influences the deformation. CNT forests have anisotropic mechanical properties, with

126 the lateral stiffness (perpendicular to the CNT alignment) typically much less than the axial stiffness

127 [27], therefore in principle favoring greater deflection due to built-in stress gradient. Local wrinkling

128 and buckling of the CNTs in the compound microstructures indicates that the growth stress causes

129 complex mechanical deformations, which cannot be predicted by linear elasticity and the bimaterial

130 deflection model (see Fig. 4a).

131 To gain further insight into the mechanical coupling causing stress-driven bending, we designed a

132 "striped" structure where alternate catalyst/underlayer regions are coupled with a large interfacial area.

133 This structure is symmetric, so it grows straight vertically yet has significant internal stresses. As

134 shown in Fig. 4a and the neighboring insets, the faster growing CNTs deform collectively into a

135   wavelike pattern. Therefore, while the vertical growth rate of the structure is matched at the interface,

136   the faster growing side still accumulates longer CNTs and these CNTs bend and possibly buckle to

137   accommodate their additional length. This deformation mode is similar to what is observed in

138   mechanically compressed forests [28].

139   As seen in **Fig. 3a** and supplementary figure **1a**, some structures separate at the interface between

140   the differentially growing regions, due to shear stresses at the interface. In future work, this could be

141   remedied by adapting the structure design to reduce the interfacial shear stress between the segments,

142   or by using a more gradual growth rate gradient to accommodate the stress gradient, such as a three-

143   layer design as in **Fig. 1b**. However, we importantly find that structures that do not separate during

144   synthesis can withstand large subsequent deformations without failure. For instance, supplementary

145   figure **1b** shows an SEM image of an arrangement of bent pillars during compression to 50% vertical

146   strain, at which point delamination at the interface begins only where the pillars kink near their

147   midsection.

148

149

150   **CNT and catalyst morphology.**

151   The strain-engineered CNT microstructures show differing CNT density and alignment in the fast

152   and slow growing portions. In **Fig. 4a,b**, the CNTs grown from catalyst on TiN appear to have greater

153   vertical alignment influenced by the interface with the faster-growing region. On the other hand, the

154   CNTs grown from catalyst on SiO_2 are less aligned, due to the retarding force from the slower-

155   growing mating regions.

156   We hypothesized that the differential CNT growth behavior on the TiN underlayer may be

157   attributed to differences in the catalyst morphology, which can influence the CNT diameter

158   distribution and number density. Atomic Force Microscopy (AFM) showed that as-deposited catalyst

159   layers on SiO_2 and TiN have a similar topology (supplementary figure **2**). However, upon annealing in

160   H_2/He prior to hydrocarbon exposure (see methods), the TiN-catalyst layer forms shallow mounds,

161   tens of nanometers high and hundreds of nanometers wide, in addition to smaller catalyst particles.

162   The control case of catalyst on SiO_2 does not exhibit such topography. For samples with 80 nm TiN

163   layer, the average catalyst particle height and spacing were calculated to be 5.2 nm and 19 nm

164   respectively. Compared to those on SiO_2 (7.5 nm and 18 nm, respectively [29]), the catalyst particle

165   sizes are smaller on average while the spacing is comparable.   In addition, the Root Mean Square

166   (RMS) roughness of the annealed catalyst/TiN layer is 5.6 nm, which is considerably higher than that

167   of catalyst on SiO_2 (1.4 nm).

168   Small Angle X-ray Scattering (SAXS) was used to further investigate the CNT forest morphology

169   [30, 31]. For this experiment, CNTs were grown for 10 minutes on SiO_2, and on 40 nm, and 80 nm

170   TiN layers; these samples reached lengths of 800, 500, and 400 μm respectively. The scattered X-ray

171   intensities were fitted to a mathematical form factor model for hollow cylinders [32] to calculate the

172 diameter and Herman's orientation parameter, which is a measure of alignment. Both the CNT

173 diameter (**Fig. 4e**) and alignment (supplementary figure **3**) are shown to be lesser for increasing TiN

174 underlayer thickness. Specifically, CNTs on SiO_2 have initial average diameter of 9.5 nm, while CNTs

175 on TiN are approximately 8 nm in diameter. These measurements further support the AFM data which

176 showed that the catalyst particles on TiN layers are smaller than those on SiO_2. The decrease in

177 diameter with growth time has been attributed to diffusion of the catalyst into the Al_2O_3 [30, 33]. The

178 Herman's orientation parameter increases from the top of the forest (the initial growth), then reaches a

179 maximum, and then decreases toward the bottom of the forest. This trend is typically observed for

180 CNT forests grown by CVD, and has been attributed to density variation due to collective activation

181 and deactivation of the growing CNT population [30]. The measured areal mass density of the CNT

182 forests is 0.011 mg mm^{-2} on 80 nm TiN and 0.018 mg mm^{-2} on SiO_2. Therefore, these methods

183 consistency show that placement of the TiN layer under the catalyst results in CNT forests with a

184 smaller average CNT diameter, lesser alignment of CNTs, and a lower density. Although we have not

185 directly compared the mechanical properties of the different segments, we expect that the CNT forests

186 on TiN have lower stiffness, and lesser anisotropy in mechanical properties. The positive correlation

187 between CNT density and alignment is also expected based on recent literature, which demonstrated

188 that CNT-CNT crowding controls alignment within non-patterned forests [34].

189

190

191 **Discussion**

192

193 **Complex 3D microstructures**

194 Based on our understanding of the elementary catalyst/underlayer designs that achieve

195 unidirectional bending, we designed a variety of more complex patterns that produce exemplary CNT

196 microstructures having complex curvature. For instance, a compound shape consisting of a "+"

197 catalyst microfeature with each arm offset by a rectangular TiN underlayer results in growth of twisted

198 CNT microstructures (**Fig. 5a**), resembling macroscale propellers. The first-order applicability of the

199 bimaterial bending model discussed above inspired us to evaluate the suitability of finite element

200 modeling (FEM) to predict the shapes of these structures. These were simulated using Comsol FEM

201 software as illustrated in **Fig. 5a,** capturing the uncoupled differential growth rate (**Fig. 1a**) as a 50%

202 expansion mismatch, and estimating the Young's modulus as 30 MPa for the CNTs on TiN and 50

203 MPa on SiO_2 [35].

204 Similarly, thin semicircles of CNTs can be directed to curve outward by offsetting the TiN

205 underlayer as shown in **Fig. 5b**. Further structural complexity is shown by the scrolling of thin offset

206 rectangular patterns (**Fig. 5c**). Last, exotic hierarchical arrangements can be formed by the interaction

207 of closely spaced structures, such as the self-organization of offset circular micropillars into wavy

patterns (**Fig. 5d**) that are reminiscent of macroscale crochet stitching. We hypothesize that, after the individual structures bend unidirectionally and contact one another, their continued growth and steric hindrance causes the wavy pattern to form. More investigation is needed to understand the complex deformations of these structures, and their relationship to the mechanics of the CNT forest and the mechanical feedback on the growth process itself.

Notably, in spite of the complex geometries and local deformations, all of these structures can be produced with impressive consistency over large arrays. Arrays of several hundred structures were examined and shown to exhibit nearly identical forms, with defects most frequently arising from debris due to the lithography process rather than the CNT growth step. In this study, we explored structures with critical dimensions as small as 5 μm (**Fig. 5**), and found that the uniformity of the structures was not sacrificed at this scale. We expect that smaller 3D microstructures could be made while still using optical lithography along with high-precision alignment of the catalyst and TiN layers. Notably, sub-micron vertical CNT features have been fabricated for use as interconnects [36]. Further, because the curved and twisted geometries result from collective behavior of CNT forest growth, we expect the structures to require a certain minimal size to average out the stochastic variation of individual CNT growth rate and catalyst lifetime. Considering the approximate CNT-CNT spacing within the current microstructures (~100 nm), the minimal feature size of reliable growth of curved microstructures may be limited to ~1 μm, though this requires further investigation.

Post-processing and mechanical reinforcement

Last, we show that 3D CNT structures can be post-processed via both wet and dry methods that enable tuning of their properties and functionality. Low-density bent CNT micropillars can be transformed into robust densely packed CNT structures by capillary forming (**Fig. 6a-b**) [35, 37, 38]. To do so, the substrate is exposed to a stream of heated acetone vapor, causing acetone to condense onto the CNTs and substrate, and infiltrate each CNT microstructure. Upon subsequent evaporation of the acetone, the CNT forest shrinks laterally, due to the surface tension of the shrinking meniscus. Previously, we showed that capillary forming of vertical CNT microstructures increases the Young's modulus in compression approximately 100-fold, from ~50 MPa to 4 GPa [35]. These values are comparable to soft rubbers and stiff epoxies, respectively. Moreover in the present case the capillary forming process preserves the curved geometry and increases the lateral deflection.

Alternatively, curved CNT microstructures can be coated conformally via vapor phase methods, thereby enabling decoupled control of geometry and mechanical properties. To investigate this, we fabricated CNT "microtruss arrays" (**Fig. 6c-e**), which are analogous to truss designs used in composite materials to achieve high strength and energy absorption at relatively low density [40-42]. The CNT microtrusses each consist of four corner members and a central pillar, meeting at an apex. We explored coating of the CNT microtrusses with both parylene (by chemical vapor deposition, CVD, supplementary figure 4) and alumina (by atomic layer deposition, ALD, **Fig. 6d**). Upon vapor

245 phase infiltration of the precursors, the CNTs and bundles within the forest are coated individually and

246 conformally [43], enabling fine-tuning of their porosity and mechanics without altering the

247 microstructure geometry. Via flat punch compression testing, we found that a 51 nm Al_2O_3 coating on

248 the CNTs increases the mechanical stiffness by more than 100-fold; typical loading-unloading curves

249 are shown in **Fig. 6e** and supplementary figure 4 for different coating materials and thicknesses. The

250 equivalent stiffness range of the 3D CNT microtrusses is 0.36 to 54 kN m^{-1}, which spans typical values

251 of MEMS springs used in probe card arrays [44]. A further attribute of the TiN underlayer is its

252 electrical conductivity. In the future, electrical integration of strain-engineered CNT structures in

253 conjunction with the post-processing methods described above could be useful in advanced

254 microsystems, including as structural elements or microsensors [45, 46]. Such applications could take

255 advantage of the thermal and mechanical durability of CNTs, as well as the anisotropic properties

256 arising from their alignment and collective curvature.

257 The ability to fabricate large arrays of 3D microstructures is also conducive to mimicry of nature's

258 advanced functional materials [5]. We say this because the structures shown in Fig. 2 and 5 have

259 similar size and geometry to butterfly wings that have anisotropic wetting properties [47], dry

260 adhesive contacts on the legs of beetles and gecko lizards [3], and microscale sensing hairs found on

261 spiders [39]. Therefore, we suggest that 3D CNT microstructures offer opportunities to further

262 engineer the excellent dry adhesive [48, 53] and superhydrophobic [54] properties previously reported

263 for CNT forests. For mechanical applications such as dry adhesion, an important consideration is the

264 adhesion of the structures to the substrate, as well as the mechanical resilience of the structures upon

265 repeated loading. While we have found that the segments of the curved structures are well adhered to

266 each other (supplementary figure **S1b**), we anticipate that coating or transfer steps may be necessary

267 to anchor the structures for use as robust surface contacts [48]. Exploration of potential optical and

268 photonic applications would require further miniaturization of the structures. Nevertheless, combined

269 with the emerging methods to grow and pattern CNT forests on large-area substrates [49-51], we are

270 optimistic that the methods shown here can enable large-area surface coatings having advanced

271 functionalities.

272

273 In summary, we show that strain-engineered CNT growth enables the scalable fabrication of

274 complex 3D microstructures having unidirectional and multidirectional curvature. The capability to

275 produce such structures *en masse* using only 2D patterning methods along with standard thermal

276 processing contrasts the limitations of many existing processes that require serial processing or

277 sequential exposure using complex inclined lithography methods. Moreover, the structures can profit

278 from the mechanical robustness and electrical conductivity of CNTs, and their mechanical and surface

279 properties can be engineered independently from their geometry by conformal coating of the CNTs

280 after growth. This represents a highly attractive principle for materials design, and is promising for

281 scalable manufacturing of 3D microstructured surfaces having biomimetic properties.

296   **Author Contributions**

297   M.D.V., S.H.T. and A.J.H. conceived the research topic. All authors designed the experiments.

298   M.D.V., S.J.P., and S.H.T. fabricated and characterized the materials. S.J.P. performed simulations.

299   All authors discussed the results, wrote and reviewed the manuscript.

300

Methods

<u>Substrate patterning and CNT growth</u>

The catalyst and TiN layers are patterned on (100) silicon wafers with 300 nm of thermally grown SiO$_2$. Each layer is patterned by lift-off processing, by photolithography (photoresist IX845) followed by ultrasonic agitation in acetone. The TiN layer is deposited and patterned first, and then the catalyst layer (1 nm Fe upon 10 nm Al$_2$O$_3$) is deposited and patterned. The wafer is then diced into ~1×1 cm pieces, and the substrates are placed in the quartz tube furnace, and the CNT growth is performed. The recipe starts by with flowing 100/400 sccm of He/H$_2$ while heating to 775 °C over 10 minutes (ramping step); then the system is held at 775 °C for 10 minutes (annealing step) while maintaining the gas flow. Then 100 sccm of C$_2$H$_4$ is added to the gas mixture at 775 °C for CNT growth for the desired duration. The typical growth rate is ~50 μm/minute on Fe/Al$_2$O$_3$/SiO$_2$. Once the CNTs have grown, C$_2$H$_4$ is removed from the gas mixture and the furnace is cooled to <100 °C. After cooling, the system is purged with He before the sample is removed. Optionally, C$_2$H$_4$ flow can be maintained while cooling down to improve the adhesion of the CNT microstructures to the substrate. Once the cooling step is complete, the quartz tube is purged with 1000 sccm of He for 5 minutes before opening up the end caps and retrieving the samples.

<u>Small Angle X-ray Scattering (SAXS):</u>

SAXS characterization of CNT microstructures was performed at the Cornell High Energy Synchrotron Source (CHESS) using the G1 beamline (10±0.1 keV, 0.13nm wavelength). The beam is focused to a 10μm spot using a single bounce monocapillary. The CNT sample is placed on a motorized stage and the focused X-ray beam is passed through the sample. The scattered beam is collected using a 2D detector and the measured intensities were normalized to the original intensity measured by another detector at upstream of the CNT sample. The scattering data is then fitted to a mathematical model assuming a log-normal distribution of hollow cylinders to calculate the CNT diameters as well as the Herman's parameter for CNT alignment. The detailed procedure is described by Bedewy et al. [30].

Figure Captions
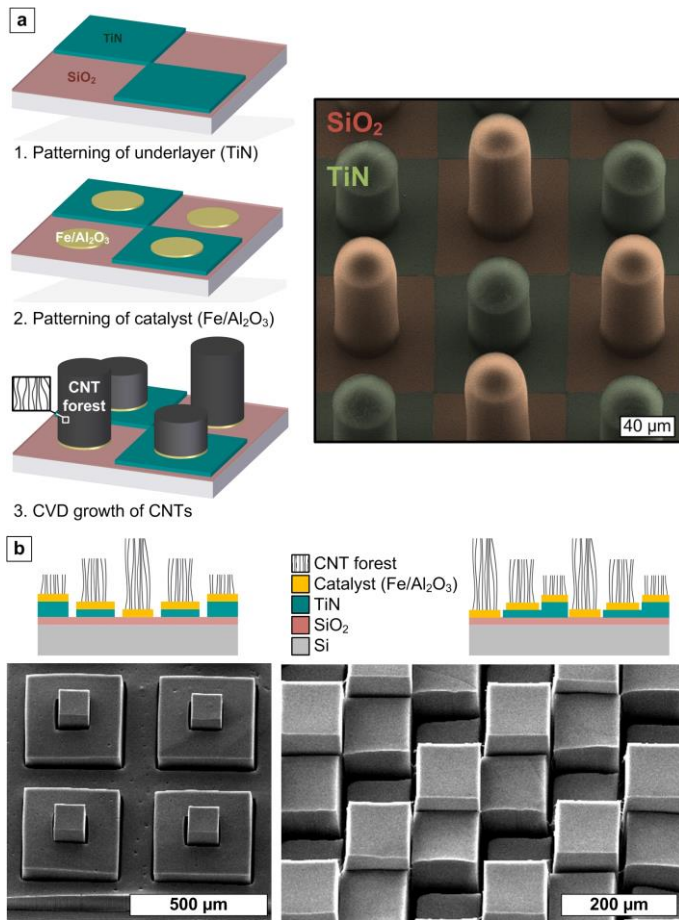
Figure 1. Multi-height CNT micropillar growth using TiN as a rate-controlling catalyst underlayer. (a) Process steps including two lithography steps, and accompanying (color added) pattern of cylindrical CNT micropillars grown on "checkerboard" of alternating TiN (80nm thickness) squares on SiO_2. (b) Triple-height arrays made by substrate and catalyst patterning with three lithography (TiN layers are 40 nm and 80 nm thickness).

338
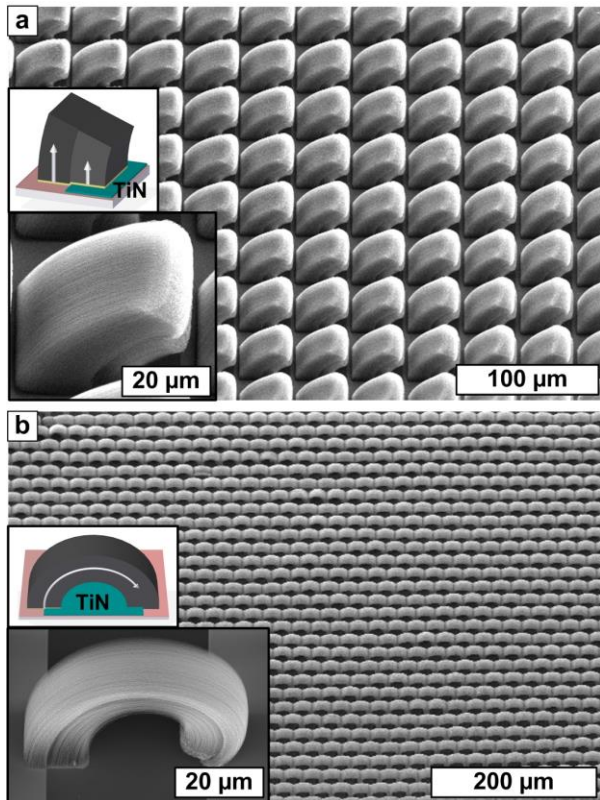
**Figure 2.** Curved CNT micropillars grown from catalyst rectangles partially overlapping TiN. The pillars bend toward the TiN side, which grows more slowly and couples to the faster-growing region of catalyst directly on SiO_2. (a) Closely-spaced short structures with ~45° takeoff angle. (b) Arch-like structures that curve over and contact the substrate at their distal ends.

343
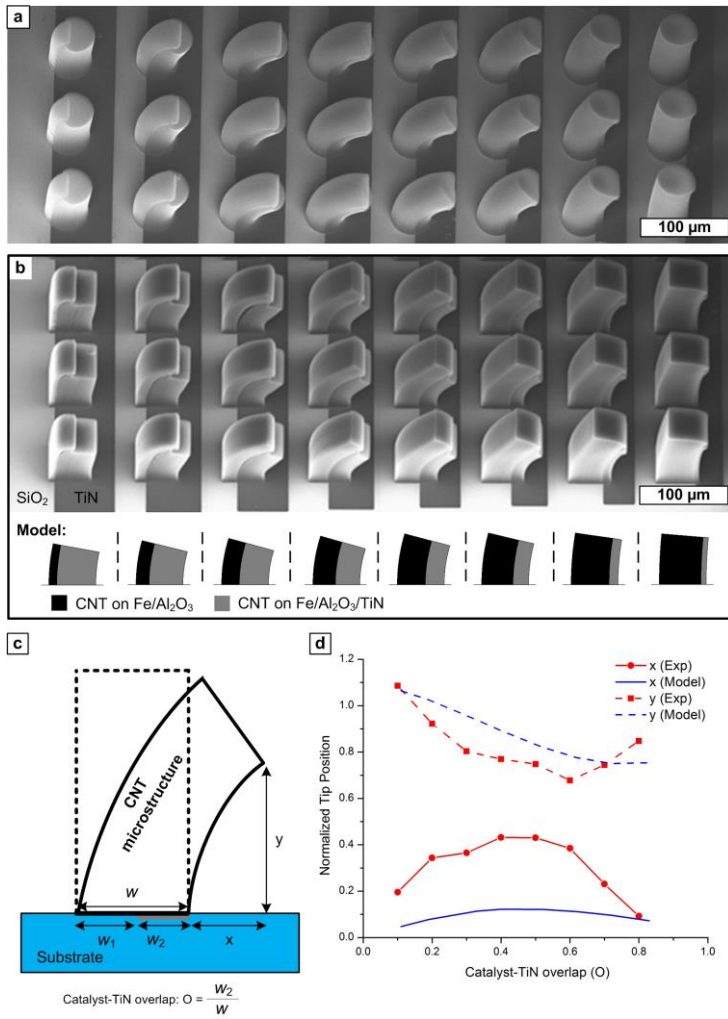
Figure 3. Shape gradients and their use in elementary modeling of the stress-driven CNT growth process. (a,b) arrays of round and square CNT micropillars with decreasing catalyst/TiN overlap from left to right. (c) Schematic of geometric parameters used to quantify deformation of square micropillars. (d) Output of differential expansion model predicting vertical and lateral deflection versus substrate pattern design, comparing simulations, inset to (b), and measurements from SEM images.
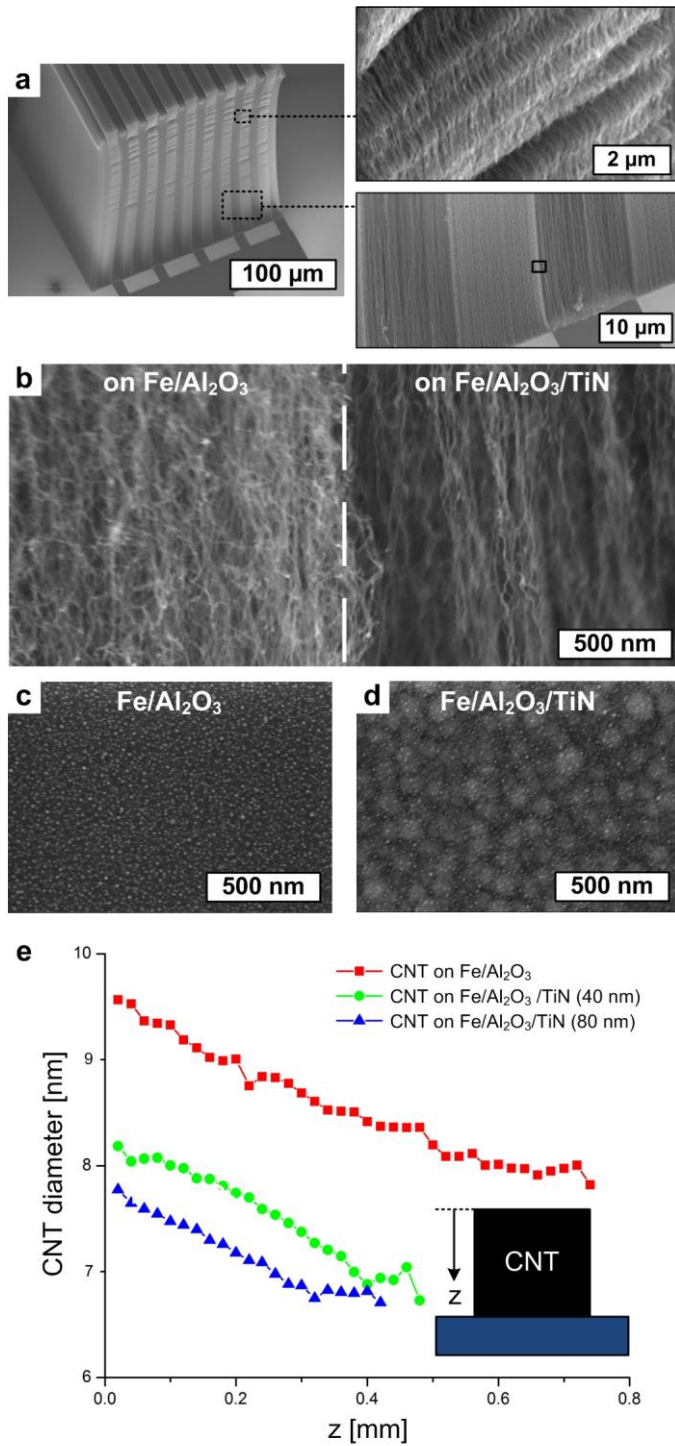
Figure 4. Analysis of CNT morphology. (a) SEM image of micropillar with catalyst on fine stripes of TiN, with close-up images showing the CNT morphology difference and evidence of internal stress causing local deformation. (b) Close-up images of the aligned CNT morphology in adjacent segments of the micropillar. (c,d) SEM images of the substrate morphology after annealing in H_2 and rapid cooling, showing hierarchical morphology of nanoparticles on the catalyst/TiN area. (e) Diameter mapping within the CNT forests, from fitting of SAXS data.
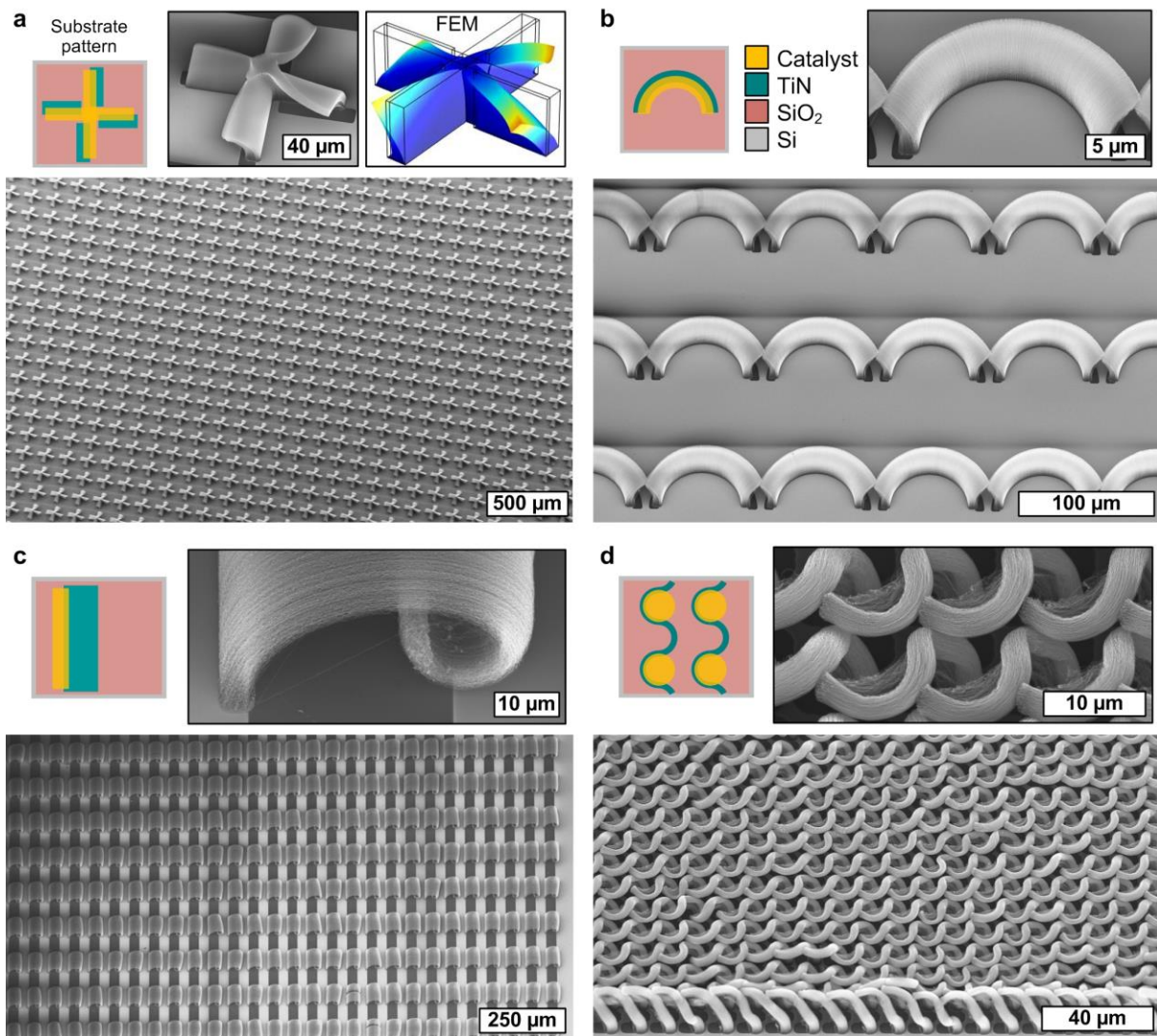
Figure 5. Design and fabrication of arrays of complex microstructures. Each of the four panels contains a sketch (top left) of the catalyst-TiN pattern used for CNT growth, a close-up SEM image (top right), and and an exemplary array of structures (bottom). (a) Twisted propeller-like structures, made from azimuthally offset crosshair catalyst/TiN layers, also compared to finite element model (FEM) prediction of shape (top right). (b) Outward curving semicircles made from radially offset catalyst/TiN layers. (c) Scroll-like deformation of thin-walled microstructures with slight catalyst/TiN overlap. (d) Collective organization of bending microstructures into a wavy pattern.

359
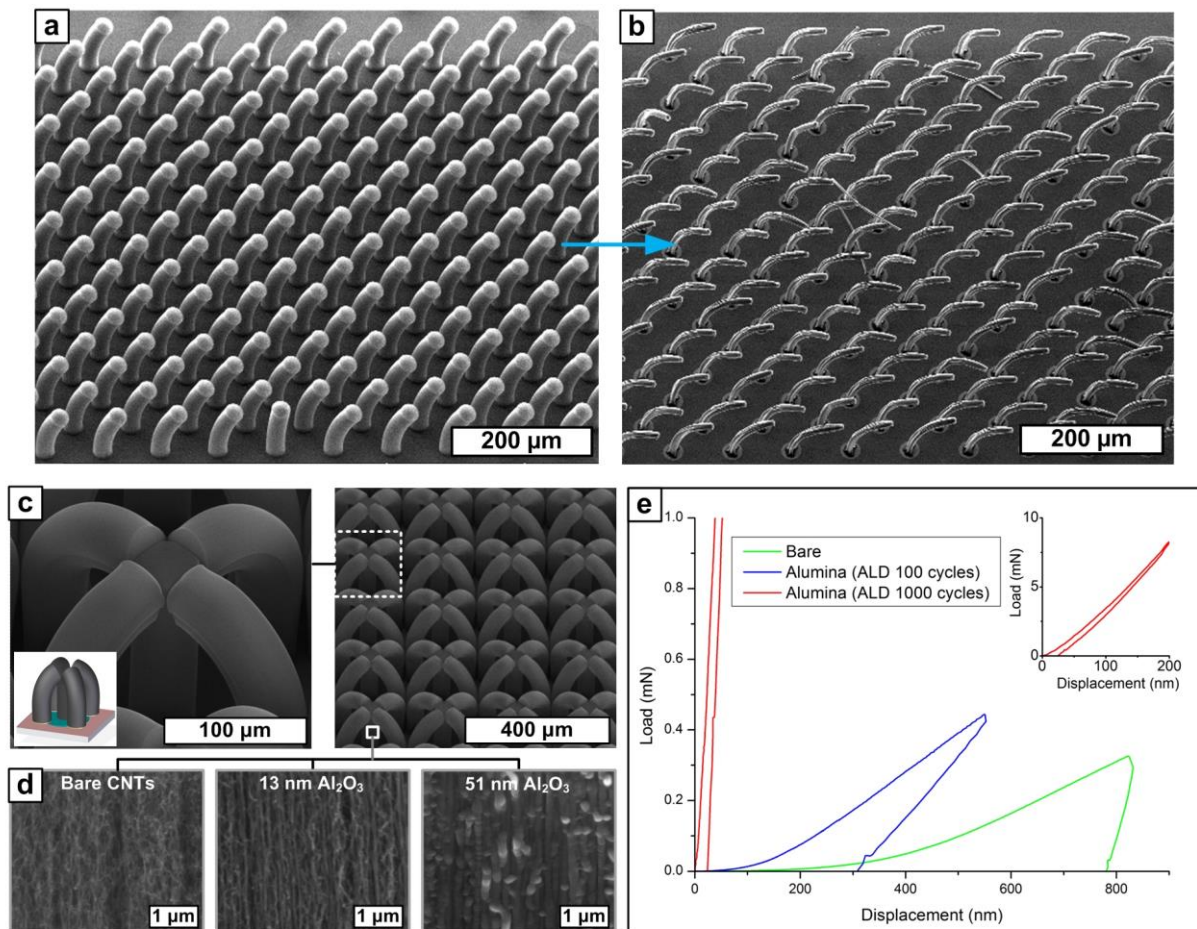
Figure 6. Post-processing of 3DCNT microstructures. (a, b) Array of bending micropillars before and after capillary forming, respectively. The unidirectional anisotropic morphology is maintained and the micropillar cross section decreases, while the lateral deflection angle of the structures increases. (c) Microtruss array fabricated to study mechanical reinforcement by vapor-phase coating of the CNTs. (d) SEM images of aligned CNTs in the forest sidewall before and after coating with Al_2O_3 by ALD. (e) Load-displacement curves before and after ALD coating, where the stiffness is measured from the slope of the unloading curve.

References

1. Aizenberg, J., et al., *Skeleton of Euplectella sp.: Structural hierarchy from the nanoscale to the macroscale.* Science, 2005. **309**(5732).
2. Grinthal, A., et al., *Steering nanofibers: An integrative approach to bio-inspired fiber fabrication and assembly.* Nano Today, 2012. **7**(1): p. 35-52.
3. Arzt, E., S. Gorb, and R. Spolenak, *From micro to nano contacts in biological attachment devices.* Proceedings of the National Academy of Sciences of the United States of America, 2003. **100**(19): p. 10603-10606.
4. Fratzl, P. and R. Weinkamer, *Nature's hierarchical materials.* Progress in Materials Science, 2007. **52**(8): p. 1263-1334.
5. Bae, W.-G., et al., *25th anniversary article: scalable multiscale patterned structures inspired by nature: the role of hierarchy.* Advanced materials (Deerfield Beach, Fla.), 2014. **26**(5): p. 675-700.
6. Campbell, M., et al., *Fabrication of photonic crystals for the visible spectrum by holographic lithography.* Nature, 2000. **404**(6773): p. 53-56.
7. del Campo, A. and C. Greiner, *SU-8: a photoresist for high-aspect-ratio and 3D submicron lithography.* Journal of Micromechanics and Microengineering, 2007. **17**(6): p. R81-R95.
8. Tawfick, S., et al., *Engineering of micro- and nanostructured surfaces with anisotropic geometries and properties.* Advanced materials (Deerfield Beach, Fla.), 2012. **24**(13): p. 1628-74.
9. Bertsch, A., S. Jiguet, and P. Renaud, *Microfabrication of ceramic components by microstereolithography.* Journal of Micromechanics and Microengineering, 2004. **14**(2): p. 197-203.
10. Stampfl, J., et al., *Photopolymers with tunable mechanical properties processed by laser-based high-resolution stereolithography.* Journal of Micromechanics and Microengineering, 2008. **18**(12).
11. Whitesides, G.M. and B. Grzybowski, *Self-assembly at all scales.* Science, 2002. **295**(5564): p. 2418-2421.
12. Grzelczak, M., et al., *Directed Self-Assembly of Nanoparticles.* Acs Nano, 2010. **4**(7): p. 3591-3605.
13. De Volder, M. and A.J. Hart, *Engineering Hierarchical Nanostructures by Elastocapillary Self-Assembly.* Angewandte Chemie-International Edition, 2013. **52**(9): p. 2412-2425.
14. Futaba, D.N., et al., *Dual Porosity Single-Walled Carbon Nanotube Material.* Nano Letters, 2009. **9**(9): p. 3302-3307.
15. De Volder, M.F.L., et al., *Corrugated Carbon Nanotube Microstructures with Geometrically Tunable Compliance.* Acs Nano, 2011. **5**(9): p. 7310-7317.
16. Grzybowski, B.A., et al., *Micro- and nanotechnology via reaction-diffusion.* Soft Matter, 2005. **1**(2): p. 114-128.
17. Noorduin, W.L., et al., *Rationally Designed Complex, Hierarchical Microarchitectures.* Science, 2013. **340**(6134): p. 832-837.
18. Scherer, M.R.J. and U. Steiner, *Efficient Electrochromic Devices Made from 3D Nanotubular Gyroid Networks.* Nano Letters, 2013. **13**(7): p. 3005-3010.
19. Pokroy, B., et al., *Self-Organization of a Mesoscale Bristle into Ordered, Hierarchical Helical Assemblies.* Science, 2009. **323**(5911): p. 237-240.
20. Kang, S.H., et al., *Meniscus Lithography: Evaporation-Induced Self-Organization of Pillar Arrays into Moire Patterns.* Physical Review Letters, 2011. **107**(17).
21. Sam, E.D., et al., *Simultaneous growth of self-patterned carbon nanotube forests with dual height scales.* Nanoscale, 2012. **4**(12): p. 3746-3753.
22. Chalapat, K., et al., *Self-Organized Origami Structures via Ion-Induced Plastic Strain.* Advanced Materials, 2013. **25**(1): p. 91-95.

434 23. De Volder, M.F.L., et al., *Self-similar organization of arrays of individual carbon nanotubes*
435 *and carbon nanotube micropillars.* Microelectronic Engineering, 2010. **87**(5-8): p. 1233-1238.
436 24. Hata, K., et al., *Water-assisted highly efficient synthesis of impurity-free single-waited carbon*
437 *nanotubes.* Science, 2004. **306**(5700): p. 1362-1364.
438 25. Maschmann, M.R., et al., *Continuum analysis of carbon nanotube array buckling enabled by*
439 *anisotropic elastic measurements and modeling.* Carbon, 2014. **66**(0): p. 377-386.
440 26. Timoshenko, S., *ANALYSIS OF BI-METAL THERMOSTATS.* J. Opt. Soc. Am., 1925. **11**(3): p. 233-
441 255.
442 27. Maschmann, M.R., et al., *Continuum analysis of carbon nanotube array buckling enabled by*
443 *anisotropic elastic measurements and modeling.* Carbon, 2014. **66**: p. 377-386.
444 28. Cao, A.Y., et al., *Super-compressible foamlike carbon nanotube films.* Science, 2005.
445 **310**(5752): p. 1307-1310.
446 29. Meshot, E.R., et al., *High-Speed in Situ X-ray Scattering of Carbon Nanotube Film Nucleation*
447 *and Self-Organization.* ACS Nano, 2012. **6**(6): p. 5091-5101.
448 30. Bedewy, M., et al., *Population Growth Dynamics of Carbon Nanotubes.* ACS Nano, 2011.
449 **5**(11): p. 8974-8989.
450 31. Wang, B.N., et al., *Quantitative characterization of the morphology of multiwall carbon*
451 *nanotube films by small-angle X-ray scattering.* Journal of Physical Chemistry C, 2007.
452 **111**(16): p. 5859-5865.
453 32. Meshot, E.R., et al., *Engineering Vertically Aligned Carbon Nanotube Growth by Decoupled*
454 *Thermal Treatment of Precursor and Catalyst.* Acs Nano, 2009. **3**(9): p. 2477-2486.
455 33. Kim, S.M., et al., *Evolution in Catalyst Morphology Leads to Carbon Nanotube Growth*
456 *Termination.* Journal of Physical Chemistry Letters, 2010. **1**(6): p. 918-922.
457 34. Xu, M., et al., *Alignment Control of Carbon Nanotube Forest from Random to Nearly Perfectly*
458 *Aligned by Utilizing the Crowding Effect.* Acs Nano, 2012. **6**(7): p. 5837-5844.
459 35. De Volder, M.F.L., et al., *Fabrication and electrical integration of robust carbon nanotube*
460 *micropillars by self-directed elastocapillary densification.* Journal of Micromechanics and
461 Microengineering, 2011. **21**(4).
462 36. Chiodarelli, N., et al., *Integration and electrical characterization of carbon nanotube via*
463 *interconnects.* Microelectronic Engineering, 2011. **88**(5): p. 837-843.
464 37. De Volder, M., et al., *Diverse 3D Microarchitectures Made by Capillary Forming of Carbon*
465 *Nanotubes.* Advanced Materials, 2010. **22**(39): p. 4384-+.
466 38. Hayamizu, Y., et al., *Integrated three-dimensional microelectromechanical devices from*
467 *processable carbon nanotube wafers.* Nature Nanotechnology, 2008. **3**(5): p. 289-294.
468 39. Barth, F.G., *How to catch the wind: Spider hairs specialized for sensing the movement of air.*
469 Naturwissenschaften, 2000. **87**(2): p. 51-58.
470 40. Deshpande, V.S., N.A. Fleck, and M.F. Ashby, *Effective properties of the octet-truss lattice*
471 *material.* Journal of the Mechanics and Physics of Solids, 2001. **49**(8): p. 1747-1769.
472 41. Radford, D.D., N.A. Fleck, and V.S. Deshpande, *The response of clamped sandwich beams*
473 *subjected to shock loading.* International Journal of Impact Engineering, 2006. **32**(6): p. 968-
474 987.
475 42. Gu, S., T.J. Lu, and A.G. Evans, *On the design of two-dimensional cellular metals for combined*
476 *heat dissipation and structural load capacity.* International Journal of Heat and Mass
477 Transfer, 2001. **44**(11): p. 2163-2175.
478 43. TAWFICK, S., et al., *Nanocomposite microstructures with tunable mechanical and chemical*
479 *properties.* PHYSICAL CHEMISTRY CHEMICAL PHYSICS, 2010. **12**(17): p. 4446-4451.
480 44. Novitsky, J. and C. Miller, *Wafer-level CSP, wafer-level assembly/test: Integrating backend*
481 *processes.* Solid State Technology, 2001. **44**(2): p. 78-+.
482 45. De Volder, M., et al., *Hydrogel-driven carbon nanotube microtransducers.* Soft Matter, 2011.
483 **7**(21): p. 9844-9847.
484 46. Hutchison, D.N., et al., *Carbon Nanotubes as a Framework for High-Aspect-Ratio MEMS*
485 *Fabrication.* Journal of Microelectromechanical Systems, 2010. **19**(1): p. 75-82.

486 47. Zheng, Y., X. Gao, and L. Jiang, *Directional adhesion of superhydrophobic butterfly wings.* Soft
487 Matter, 2007. **3**(2): p. 178-182.
488 48. Rong, Z., et al., *Bio-Inspired Hierarchical Polymer Fiber-Carbon Nanotube Adhesives.*
489 Advanced Materials, 2014. **26**(9): p. 1456-1461.
490 49. Yasuda, S., et al., *Improved and Large Area Single-Walled Carbon Nanotube Forest Growth by*
491 *Controlling the Gas Flow Direction.* Acs Nano, 2009. **3**(12): p. 4164-4170.
492 50. Zhang, Q., et al., *Carbon Nanotube Mass Production: Principles and Processes.* Chemsuschem,
493 2011. **4**(7): p. 864-889.
494 51. Polsen, E.S., A.G. Stevens, and A.J. Hart, *Laser Printing of Nanoparticle Toner Enables Digital*
495 *Control of Micropatterned Carbon Nanotube Growth.* Acs Applied Materials & Interfaces,
496 2013. **5**(9): p. 3656-3662.
497 52. Mizuno, K., et al., *A black body absorber from vertically aligned single-walled carbon*
498 *nanotubes.* Proceedings of the National Academy of Sciences of the United States of
499 America, 2009. **106**(15): p. 6044-6047.
500 53. Qu, L., et al., *Carbon nanotube arrays with strong shear binding-on and easy normal lifting-*
501 *off.* Science, 2008. **322**(5899): p. 238-242.
502 54. Lau, K.K.S., et al., *Superhydrophobic carbon nanotube forests.* Nano Letters, 2003. **3**(12): p.
503 1701-1705.

504